frontiers in Materials

ORIGINAL RESEARCH
published: 17 May 2021
doi: 10.3389/fmats.2021.603820

The Influence of Clamping, Structure Geometry, and Material on Seismic Metamaterial Performance

T. Venkatesh Varma[1], *Bogdan Ungureanu*[2]*, *Saikat Sarkar*[1], *Richard Craster*[2,3,4], *Sébastien Guenneau*[4] and *Stéphane Brûlé*[5]

[1] Department of Civil Engineering, Indian Institute of Technology Indore, Indore, India, [2] Department of Mathematics, Imperial College London, London, United Kingdom, [3] Department of Mechanical Engineering, Imperial College London, London, United Kingdom, [4] UMI 2004 Abraham de Moivre-CNRS, Imperial College London, London, United Kingdom, [5] CNRS, Centrale Marseille, Institut Fresnel, Aix Marseille University, Marseille, France

OPEN ACCESS

Edited by:
Andrea Bacigalupo, University of Genoa, Italy

Reviewed by:
Antonio Salvador Gliozzi, Politecnico di Torino, Italy
Valentina Volpini, University of Modena and Reggio Emilia, Italy
Michael Nieves, Keele University, United Kingdom

***Correspondence:**
Bogdan Ungureanu
b.ungureanu@imperial.ac.uk

Specialty section:
This article was submitted to Mechanics of Materials, a section of the journal Frontiers in Materials

Received: *08 September 2020*
Accepted: *22 March 2021*
Published: *17 May 2021*

Citation:
Varma TV, Ungureanu B, Sarkar S, Craster R, Guenneau S and Brûlé S (2021) The Influence of Clamping, Structure Geometry, and Material on Seismic Metamaterial Performance. Front. Mater. 8:603820. doi: 10.3389/fmats.2021.603820

Diverting and controlling the impact of elastic vibrations upon an infrastructure is a major challenge for seismic hazard mitigation and for the reduction of machine noise and vehicle vibration in the urban environment. Seismic metamaterials (SMs), with their inherent ability to manipulate wave propagation, provide a key route for overcoming the technological hurdles involved in this challenge. Engineering the structure of the SM serves as a basis to tune and enhance its functionality, and inspired by split rings, swiss-rolls, notch-shaped, and labyrinthine designs of elementary cells in electromagnetic and mechanical metamaterials, we investigate altering the structure geometries of SMs with the aim of creating large bandgaps in a subwavelength regime. Interestingly, clamping an SM to the bedrock creates a zero frequency stopband, but further effects can be observed in the higher frequency regime due to their specific geometry. We show that square stiff inclusions perform better in comparison to circular ones while keeping the same filling fraction. En route to enhancing the bandgap, we have also studied the performance of SMs with different constituent materials; we find that steel columns, as inclusions, show large bandgaps, however, the columns are too large for steel to be a feasible material in practical or financial terms. Non-reinforced concrete would be preferable for industry level scaling up of the technology because, concrete is cost-effective, easy to cast directly at the construction site and easy to provide arbitrary geometry of the structure. As a part of this study, we show that concrete columns can also be designed to exhibit bandgaps if we cast them within a soft soil coating surrounding the protected area for various civil structures like a bridge, building, oil pipelines, etc. Although our motivation is for ground vibration, and we use the frequencies, lengthscales, and material properties relevant for that application, it is notable that we use the equations of linear elasticity, and our investigation is more broadly relevant in solid mechanics.

Keywords: seismic metamaterial, transmission diagram, dispersion curves, bandgap, geophysics, computational physics, inertial resonators, Floquet-Bloch waves

1. INTRODUCTION

Controlling elastic waves near structures is key to addressing a large class of civil engineering problems ranging from seismic hazard mitigation to stopping unwanted noise and vibration produced by vehicles, heavy machinery on construction sites, etc. (Brownjohn et al., 2011; Bajcar et al., 2012; Zhang et al., 2016; Yao et al., 2019). Seismic waves lead to the destruction of civil installations and loss of life, thus forming one of the most important and difficult challenges for civil engineers; the reduction of urban noise and vibration is also important because they create health issues and have other consequences, such as affecting highly sensitive scientific and medical instruments. There are many other applications, e.g., in the context of ground motions produced from even minor tremors, industrial machinery, or suburban rail transport systems degrading the structural integrity of nearby buildings, pipeline systems, and sensitive instruments; additionally, small-scale damage to structures in petrochemical industries or nuclear reactors can have devastating consequences. Traditional approaches for vibration mitigation, mostly in the form of base isolation (BI) and tuned mass damper (TMDs) have certain limitations (Zhou et al., 2002; Xiang et al., 2012; Xiang and Nishitani, 2014; Harvey and Kelly, 2016; Anajafi and Medina, 2018; Fabrizio et al., 2019): BI induces large movement of the structures which may not be acceptable, TMD works only for a narrow frequency range outside of which it may work adversely which is again a major issue because identifying the frequency contents in the structure correctly is not straightforward as it may change significantly with time due to structural degradation and environmental change (Moser and Moaveni, 2011; Wagner et al., 2017).

In the parallel research area of electromagnetism, there is a keen interest in composites, known as metamaterials, which are assemblies of multiple elements usually arranged in periodic patterns at subwavelength scales, that were introduced (Pendry et al., 1999) as a means to achieve effective electromagnetic properties not from the properties of the constituent materials, but from the combination of elements with given shapes and orientations, such as split ring resonators. Such periodically arranged elements take their name from the shape of the thin metal sheets they are made of that allow for artificial magnetism, not present in the constituent materials (metal surrounded by plastic, neither of which are magnetic media), through the precise manipulation of electric and magnetic components of electromagnetic field and their interplay. Indeed, the electromagnetic field is tremendously enhanced due to internal capacitance and inductance phenomena upon resonance of the thin sheets. From the highly dispersive nature of the metamaterials around the resonant frequencies of split ring resonators and other arrangements, such as swiss-rolls, it is possible to block, absorb, enhance, or even bend electromagnetic waves propagating through a doubly or triply periodic array of them, as low frequency stopbands and strong anisotropy (apparent in distorted isofrequency contours in pass bands) take place (Kadic et al., 2013).

Metamaterials have the capability of manipulating a desired range of frequency components in the propagating wave, an aspect that has been extensively used in electromagnetics, optics, and micro and nano-scale mechanics (Guenneau et al., 2007; Craster and Guenneau, 2012; Watts et al., 2012; Poddubny et al., 2013; Yang et al., 2016; Brûlé et al., 2017b, 2018b, 2019; Colombi et al., 2017; Casablanca et al., 2018; Kadic et al., 2019; Zeng et al., 2020). However, their large scale extension, which can be extremely useful in solving many of the important engineering problems, mentioned above, requires development. Recent developments have indicated that metamaterials, if designed appropriately, can indeed provide a robust solution for the manipulation of elastic waves, thanks to their ability to create large frequency bandgaps even at large scale (Brûlé et al., 2014; Del Vescovo and Giorgio, 2014; Aravantinos-Zafiris and Sigalas, 2015; Moitra et al., 2015; Ungureanu et al., 2015, 2019; Colombi et al., 2016; Diatta et al., 2016; Mosby and Matouš, 2016; Palermo et al., 2016; Liu et al., 2019; Muhammad and Lim, 2019; Sun and Xiao, 2019).

Early work by Economou and Sigalas (1993) established a generic trend that a denser inclusion in the microstructure geometry of periodic media exhibits bandgaps for 2D and 3D structures. This phenomenon is predicted in Mandelik et al. (2003), Gazalet et al. (2013), and Gómez-León and Platero (2013) by using the Floquet-Bloch theory which is applicable to different wave types traveling through a periodic media. Experimentally (Meseguer et al., 1999a,b) showed the attenuation of surface elastic waves in a marble quarry containing repeated circular holes with the bandgaps obtained in a high frequency range of several kHz which is not important for seismic applications, because seismic forces mostly contain very low frequencies in the range of few Hz (Gadallah and Fisher, 2005; Kramer, 2007; Chestler and Creager, 2017; Nakano et al., 2018). The first full-scale experiments (Brûlé et al., 2014, 2017a) to attenuate surface elastic waves, such as Rayleigh and Love waves, were conducted in structured soil and extended in Brûlé et al. (2018a, 2020), Brûlé and Guenneau (2019), and Ungureanu et al. (2019); the soil was engineered with cylindrically configured voids as inclusions in a periodic manner, and this experiment shows the feasibility of using phononic crystals and metamaterials at a meter-scale important for civil engineering applications.

A variety of extensions of these concepts are aimed at creating larger bandgaps and to force these to occur at the low frequencies required for civil engineering applications. Recently, Miniaci et al. (2016) numerically analyzed and designed optimal configuration for inclusions of micro-structure geometry, i.e., cross-shaped voids and hollow cylindrical and locally resonant inclusions (e.g., steel, rubber, and concrete), which shield low frequency contents in seismic forces. Their parametric study on the filling fraction of inclusions in microstructure shows a possibility of enhancing the bandgap. The ultimate goal of bandgap engineering in this context is to create a zero-frequency bandgap, i.e., one that starts at zero frequency and then extends over a broad range of low frequencies. Achaoui et al. (2017) show that this can be achieved with cylindrical steel inclusions clamped to a bed rock which lies underneath a soil layer; they also considered struts linking the cylindrical steel columns.

Here, we focus on large scale metamaterials made by periodically installing stiff columns in a matrix-like soil. There are

many aspects that are not yet known about such metamaterials, e.g., effect of structure geometry, that is the detailed geometry within a single building block of the periodic medium, and material constituents. Although the possibility of enhancing the bandgap *via* varying the substitution ratio of stiffer inclusions is established, the effect of varying the structure geometry and keeping the same filling-fraction, are yet to be addressed. In the present study, we investigate the effect of the structure geometry in SMs with the aim of creating large bandgaps, keeping the volume of inclusions same. As an illustrative example of the importance of both clamping and structure geometry, we consider, in **Figure 1**, two similar geometries for SMs when they vibrate freely (A,B) and when they are clamped to the bedrock (C,D). We see in **Figure 1** that just simply tilting some junctions between a cylinder and a bulk medium has a profound impact on stopband width, as noted in earlier studies on phononic crystals consisting of inertial resonators (Bigoni et al., 2013; Wang et al., 2014, 2015). Interestingly, we find that a torsional mode is associated with the upper edge of the stopband in (A,B), see **Figures 2D,H** for the case of inertial resonators (IRs) with tilted junctions (also known as ligaments). Such resonance is akin to those studied in chiral elastic metamaterials in a very different range of frequencies (Frenzel et al., 2019). Furthermore, a similar geometrical effect occurs in the higher frequency spectrum when the inclusion is clamped at the bottom. This emphasizes the importance of structure geometry as an additional mechanism to tune higher frequency band spectra of clamped SMs. We also explore the performance of SMs by considering different constituent materials. Specifically, we aim to maximize the bandgap width as well as the number of stopbands since the SMs may have to safeguard different types of civil installations with varied frequency contents ranging from massive tall buildings with very small natural frequencies to fluid conveyors containing large natural frequencies (Dym and Williams, 2007; Dym, 2012). Enroute to enhancing the bandgap, we report an innovative design for SM, which is very pertinent to civil engineering practices. The rest of the paper is organized as follows: The mathematical formulation is shown in section 2 and consequently numerically simulated results are given in section 3. Finally, we draw some conclusions in section 4.

2. MATHEMATICAL FORMULATION-FINITE ELEMENT APPROACH

We take an elastic medium consisting of isotropic homogeneous phases, for which the governing equation (Achenbach, 1973) is

$$(\lambda+\mu)\frac{\partial^2 u_j}{\partial x_j \partial x_i}+\mu\frac{\partial^2 u_i}{\partial x_j \partial x_j}=\rho\frac{\partial^2 u_i}{\partial t^2} \tag{1}$$

which is valid in each homogeneous phase which is described by a constant density ρ and Lamé parameters λ and μ. We use tensor notation. Equation (1) is supplied with a no slip condition at the interface between the homogeneous phases, i.e., relative displacement will be zero between the phases as well as continuity of the normal component of stress to the interface. We work primarily in the frequency, ω, domain and assume $\exp(-i\omega t)$ dependence is considered, understood, and suppressed henceforth.

A periodic medium can be analyzed by sequential translational operations performed on its elementary cell, by making use of a lattice vector $\mathbf{a} = (a_1, a_2)$. The inherent periodicity of this cell enables us to characterize the dispersion properties of elastic waves propagating within such a periodic medium, *via* Bloch's theorem as in Equation (2), where $\mathbf{k} = (k_x, k_y)$ is the Bloch wavevector and $\mathbf{x} = (x_1, x_2)$ (Brillouin, 2003):

$$\mathbf{u}(\mathbf{x}+\mathbf{a}) = \mathbf{u}(\mathbf{x})\exp(i\mathbf{k}.\mathbf{a}) \tag{2}$$

and to obtain dispersion relations between frequency and phase-shift, we need only consider the elementary cell (see e.g., Guenneau and Movchan, 2004).

For our numerical simulations, we arrive at Equation (3) by discretizing u in weak form using 3D shape functions in a finite element approach (Reddy, 1993): **K** and **M** being global stiffness and mass matrices, respectively, which are basically functions of Bloch wavevector **k**, and **U** is the assembled displacement vector:

$$(\mathbf{K}-\omega^2\mathbf{M})\mathbf{U} = \mathbf{0} \tag{3}$$

where **0** is the null vector.

Floquet-Bloch analysis is conducted by computing dispersion curves *via* varying $\mathbf{k} = (k_x, k_y)$ along the edges of irreducible Brillouin zone (IBZ). For a square lattice, IBZ lies along the edges of the triangle ΓMX; $\Gamma = (0,0)$, $M = (\frac{\pi}{a}, \frac{\pi}{a})$, and $X = (\frac{\pi}{a}, 0)$, where $a = a_1 = a_2$. For a real valued **k**, the frequencies (ω) are obtained by solving an appropriate eigenvalue problem, thereby constructing the dispersion curves *via* plotting real valued frequencies corresponding to **k** (Van Der Aa et al., 2007; Jarlebring et al., 2017). Since dispersion curves are computed over a medium representing an infinite array of microstructured geometry, they alone do not fully reveal the inherent effectiveness of SM design. For this purpose, transmission spectra are also computed, which is a measure of wave propagation attenuation/transmission losses over a finite medium (Lee and Wu, 2010).

3. RESULTS AND DISCUSSION

In this section, we present dispersion curves and transmission losses for different microstructure geometries. We have already illustrated the importance of microstructure geometry with cylindrical inertial resonators that make possible a torsional mode associated with a large stopband of around 50 Hz when IRs are freely vibrating, see **Figures 1B**, **2D,H** in section 1. Clamping IRs to the bedrock suppress all ground vibrations below 13 Hz but prevent the appearance of the torsional mode, and so the stopband at 50 Hz disappears. We further note that tilting the ligaments of IRS of both the freely vibrating (**Figure 1B**) and clamped (**Figure 1D**) cases, opens a high frequency stopband around 83 Hz. Depending upon applications (e.g., earthquake protection which is mostly in the 0–10 Hz range, or, for instance, suppression of ground vibration due to car and railway traffic, which is concerned with higher

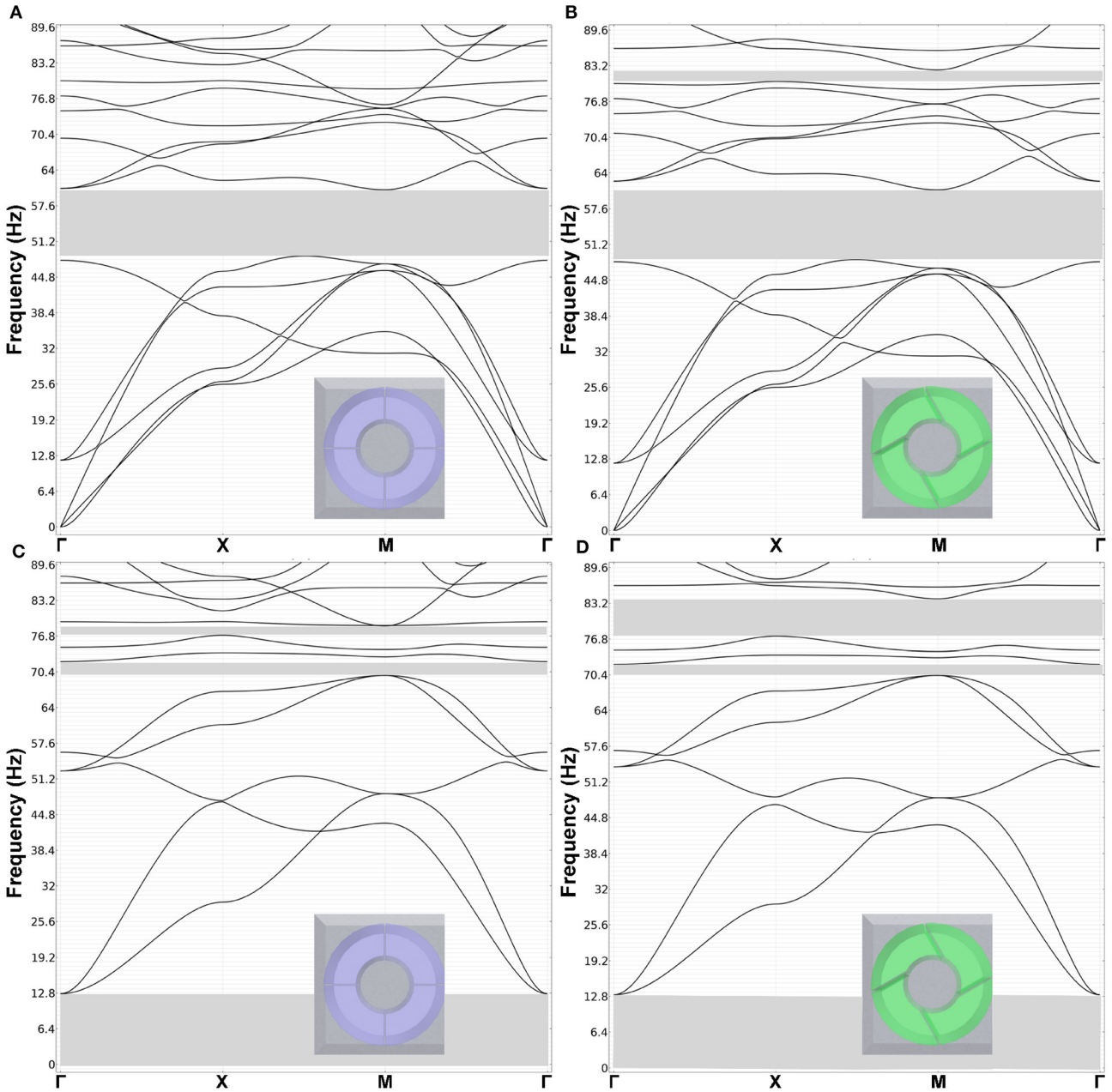

FIGURE 1 | Floquet-Bloch band diagrams for cylindrical inclusions obtained for a modulus of Bloch wavevector | **k** |, see (2), that describes the edges of the irreducible Brillouin zone Γ*XM*. Note that there is an enhanced bandgap range for inclusion with four aligned ligaments **(A)** in comparison to cylindrical inclusion with inclined ligaments **(B)**: the bandgap width is ∼12 Hz for the former and 15 Hz for the latter, in accordance with earlier study on 2D inertial resonators (Bigoni et al., 2013). Note also that a new gap is opening around 80 Hz. However, when we clamp the inertial resonators in **(A,B)** to the bottom of the plate (that could be a model for a bedrock), in **(C,D)**, respectively, we note some zero frequency stopbands occur between 0 and 12.8 Hz, and the first three bands in **(A)**, **(B)** do not appear in **(C,D)**. This is the clamping effect already observed in Achaoui et al. (2017). Importantly, the rotational modes occur at frequencies below the first stopband (see also **Figures 2A–F**). Indeed, the localized mode associated with lower edge of first stopband in **(A)**, **(B)** is a longitudinal mode (see **Figures 2C,G**). The localized mode associated with upper edge of first stopband in **(A)**, **(B)** is a torsional mode (it rotates clockwise on top of plate and counterclockwise on bottom of plate) (see **Figures 2D,H**), and is not excited in the clamped case, which only depicts a high frequency stopband.

frequencies), civil engineers might focus on clamping to bedrock, or on micro-structure geometry, of SMs. Thus, there is certainly a trade-off between micro-structure geometry and clamping that needs to be taken into account in the design of clamped SMs in order to achieve optimal performance in range of frequencies of interest. To the best of our knowledge, this has

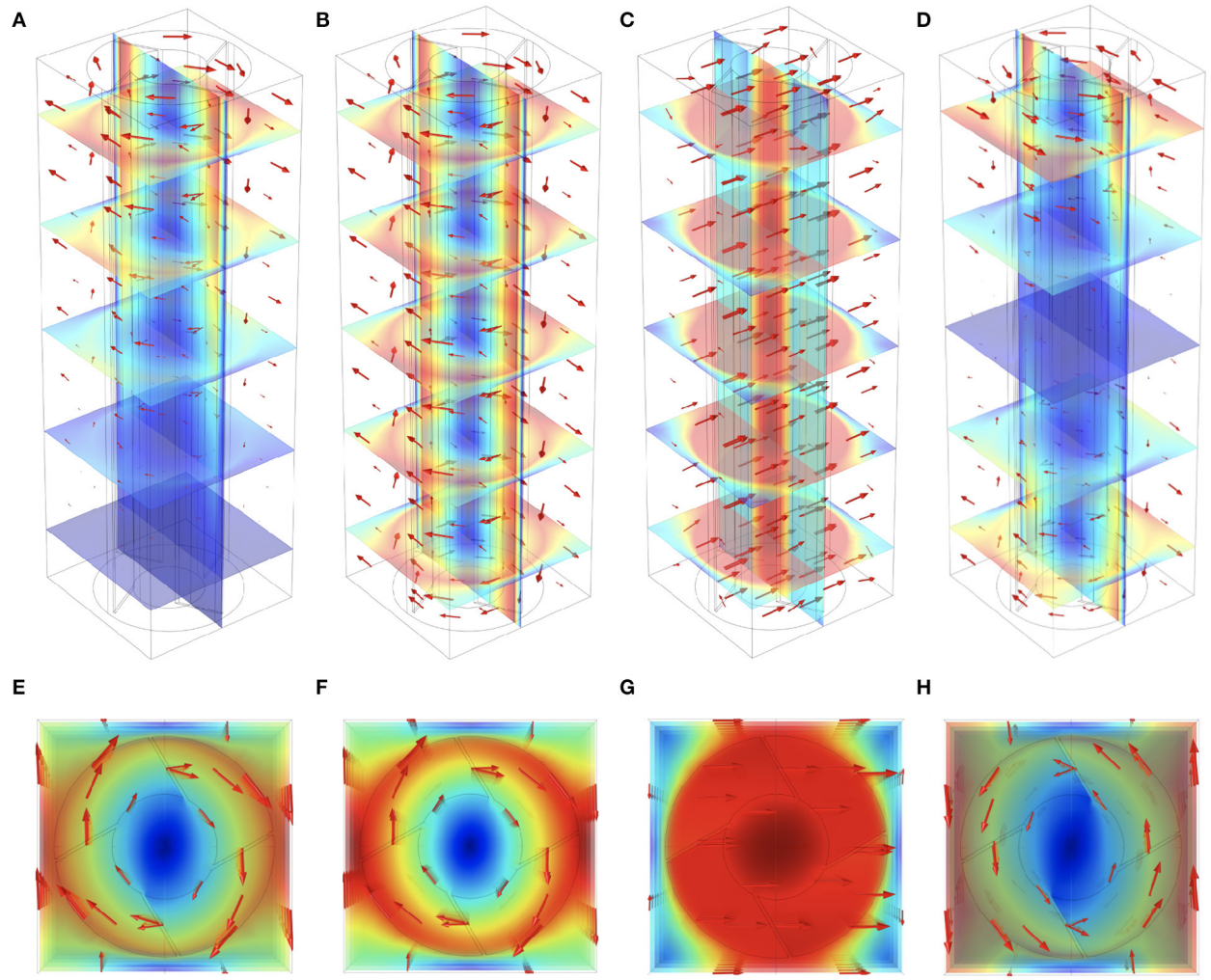

FIGURE 2 | Representative eigenmodes for cylindrical inertial resonators (IRs) with four inclined ligaments at high-symmetry point X of the irreducible Brillouin zone Γ*XM*: **(A,E)** Rotational mode at 48.5 Hz (IR clamped at bottom, third mode in **Figure 1D**); **(B,F)** Rotational mode 38.6 Hz (fourth mode in **Figure 1B**); **(C,G)** Longitudinal mode at 45.8 Hz (sixth mode in **Figure 1B**); **(D,H)** Torsional mode at 63.8 Hz (seventh mode in **Figure 1B**).

never been studied before, and this is the main scope of the present section.

To arrive at a microstructure that maximizes the bandgap (with or without clamping), we compare different results keeping the substitution ratio the same. Having arrived at a particular configuration, we explore the effect of changes in orientation of the inclusion from 0 to 45°. After this, we move to the aspect of material constituent for the inclusion, and we also focus on cost-effectiveness and ease of fabrication of arbitrary microstructure geometry.

3.1. Comparison of Different Geometry of Inclusions

Most standard civil engineering infrastructures are constructed on medium to dense soil, for their obvious stability purposes, and to reflect this, we choose realistic soil conditions, i.e., medium soil with parameters as elastic modulus, E = 153 MPa, Poisson's ratio, $\mu = 0.3$, and density, and $\rho = 1{,}800$ kg/m^3. The microstructure of the periodic media is configured with steel columns as inclusions in three forms having the same substitution ratio as shown in **Figure 3**.

- Cylindrical steel column of height 10 m and circular cross-section of radius 1.128 m.
- Regular-sized square steel column of same height, i.e., 10 m. The cross-section of regular-sized square is taken as 2 × 2 m.
- Notch-shaped square steel column again with same height, i.e., 10 m. 0.4 × 0.6 m notch is provided in a square of 2.25 m size as shown in **Figure 3E**.

Each form of inclusion is embedded in unstructured medium soil matrices (3 × 3 × 10 m) so as to make an elementary cell that forms the microstructure of the periodic media; the

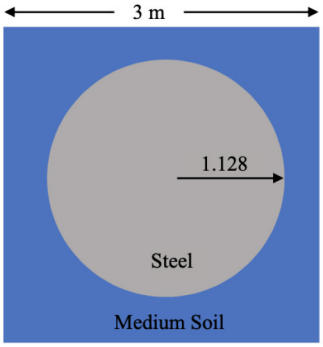

A Cross-section of cylindrical steel inclusion with 0.445 substitution ratio

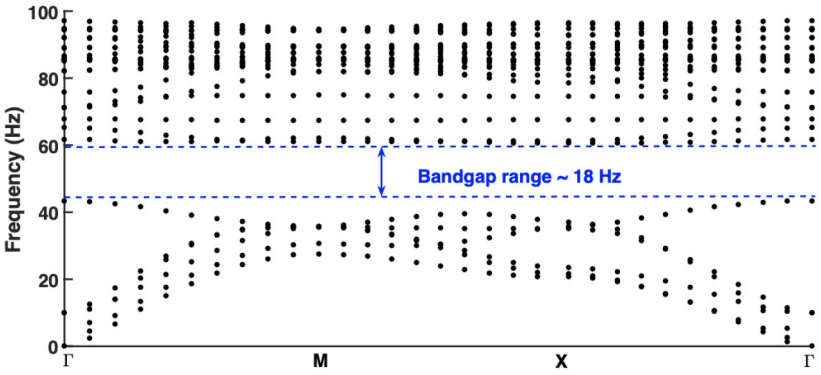

B Dispersion curves for cylindrical inclusion

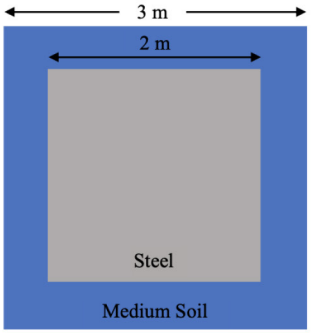

C Cross-section of regular square steel inclusion with 0.445 substitution ratio

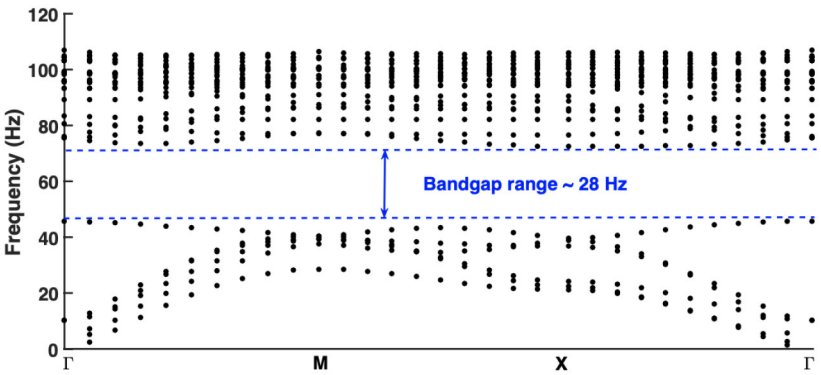

D Dispersion curves for square inclusion

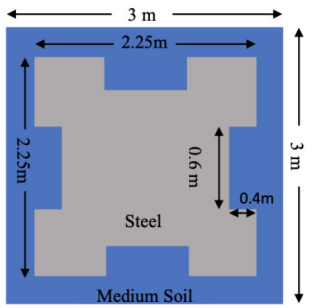

E Cross-section of notch-shaped square steel inclusion with 0.445 substitution ratio

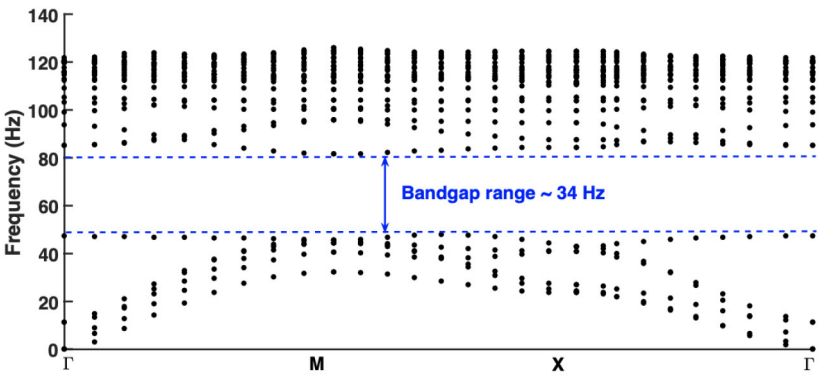

F Dispersion curves for notch-shaped square inclusion

FIGURE 3 | Unclamped configuration of **(A)** cylindrical ($r = 1.128$ m, $h = 10$ m), **(C)** regular-shaped square ($2 \times 2 \times 10$ m) and **(E)** notch-shaped square geometry inclusions in the elementary cell ($3 \times 3 \times 10$ m) of periodic media (medium soil) with equal substitution ratio (0.445). Dispersion curves for **(B)** cylindrical **(D)** regular-shaped square, and **(F)** notch-shaped square inclusions are obtained around the edges of the irreducible Brillouin zone Γ*XM*. Note that there is an enhanced bandgap range with regular-shaped square (~28 Hz) and notch-shaped square (~34 Hz) inclusions in comparison to cylindrical inclusion (~18 Hz).

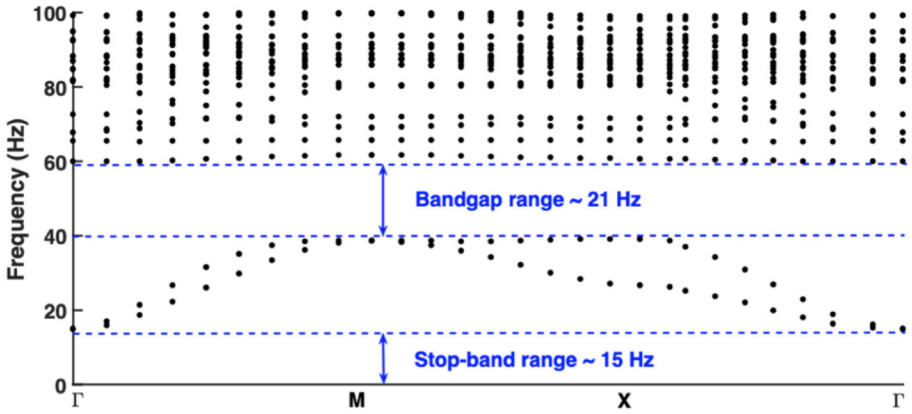

A Dispersion curves for circular cross-section with 1.128 m radius as shown in **Fig. 3a**

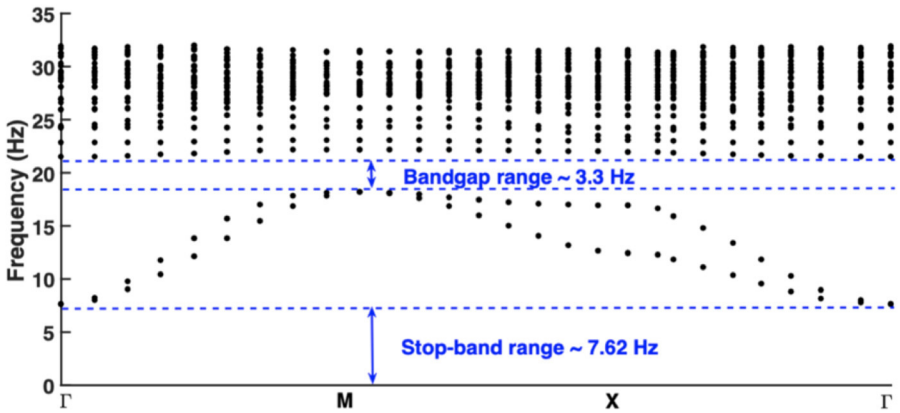

B Dispersion curves for regular-shaped square cross-section of side length 2 m as shown in **Fig. 3c**

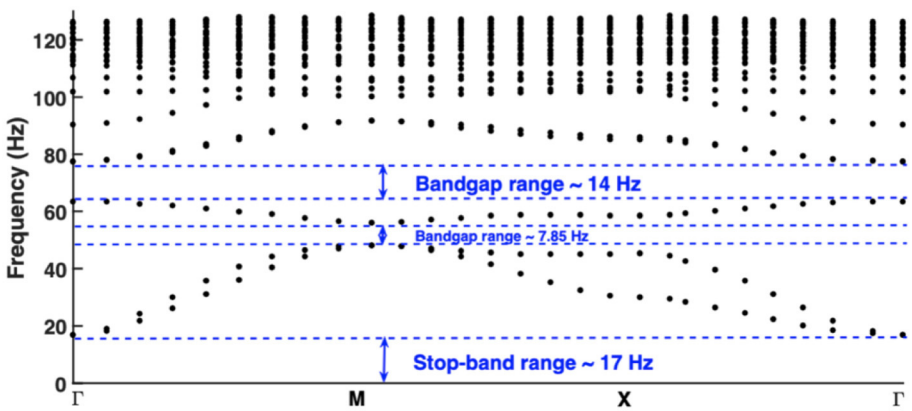

C Dispersion curves for notch-shaped square cross-section (four notches of dimension 0.6 x 0.4 m in a 2 m square as shown in **Fig. 3e**)

FIGURE 4 | Dispersion curves for clamped configuration of geometries, i.e., the base of the inclusion column is clamped, shown in **Figure 3** with the same substitution ratio 0.445. Notch-shaped square cross-section shows a higher stopband than the other two geometries, however, the frequencies are lifted up in their comparison. **(A)** Dispersion curves for circular cross-section with 1.128 m radius as shown in **Figure 3A**. **(B)** Dispersion curves for regular-shaped square cross-section of side length 2 m as shown in **Figure 3C**. **(C)** Dispersion curves for notch-shaped square cross-section (four notches of dimension 0.6 × 0.4 m in a 2 m square as shown in **Figure 3E**).

top and bottom of the microstructure remain unclamped for the simulations shown in **Figure 3**. Elastic properties of steel are chosen as $E = 200$ GPa, Poisson's ratio, $\mu = 0.33$, and density, $\rho = 7{,}850$ kg/m^3. We have also used soft clay models (which will be seen subsequently) to study the effect of soil on bandgap enhancement. A comparison of its dispersion properties, obtained along the edges of the irreducible Brillouin zone ΓMX (see section 2), can be made from **Figure 3**. Bandgaps are obtained in all the configurations, i.e., microstructure with inclusions having circular, regular square, and notch-shaped square cross-sections. The square cross-section inclusions show higher range of bandgaps (∼28 and 34 Hz in regular and notch-shaped, respectively) in comparison to circular cross-section inclusion (∼18 Hz) for the same substitution ratio of steel.

Comparison of stopbands for these configurations are also obtained (see **Figure 4**) by clamping the bottom of the microstructure. Here, the column inclusions with circular cross-sections show better zero-frequency stopbands (with upper limit at ∼15 Hz) in contrast to regular square-shaped inclusions (upper limit at ∼7.62 Hz). However, the notch-shaped square inclusion shows a slightly higher stopband (upper limit ∼17 Hz) to that of circular cross-section for the same substitution ratio of steel inclusion. Along with the zero-frequency stopband, there is an additional bandgap at a higher frequency range that is also observed for all three forms of inclusions. The circular cross-section shows a higher frequency bandgap with a range of around 21 Hz in comparison to the regular square-shaped cross-section which has only a narrow bandgap with a range of about 3.3 Hz. The notch-shaped square cross-section shows a slightly higher range of bandgaps, ∼21.75 Hz (7.85 + 14 Hz) than the circular cross-sectioned inclusion. However, the bandgaps for circular and notch-shaped inclusions are positioned in the higher frequency spectrum, which are less important for engineering applications.

Motivated by the literature on electromagnetic metamaterials, other investigated micro-structure geometries are now considered: coil/labyrinthine (complex sheet piling type of inclusion), split ring-like, and swiss roll-like cylindrical steel inclusions in medium soil (see **Supplementary Figures 2, 3**). The same substitution ratio, i.e., 0.445 was considered as in the former two microstructures, whereas the swiss roll-like inclusion is considered with a diameter equal to that of the solid circular inclusion in **Figure 3**, i.e., 1.128 m with a substitution ratio of 0.15. Notably, in medium soil, without clamping the bottom, a split-ring like inclusion with four gaps shows a bandgap of ∼10.6 Hz, whereas the labyrinthine inclusion shows no bandgap. Testing with other material constituents for a labyrinthine inclusion (**Supplementary Figure 2a**), i.e., with rubber and concrete, no bandgap was observed (see **Supplementary Figure 4**). On the other hand, split-ring with two gaps shows an enhanced bandgap (12 Hz in the range of 46.84–59.23 Hz) as compared to a four gap split-ring (10.6 Hz in the range of 48.53–58.35 Hz) with the same substitution ratio (0.445). Dispersion curves for swiss roll-like steel inclusion with different thickness, i.e., 0.128 and 0.03 m in medium soil ($3 \times 3 \times 10$ m) is obtained by without clamping the bottom and is shown in **Supplementary Figure 3**. Clearly, there is no bandgap for these configurations.

The stopbands for the configurations in **Supplementary Figures 2, 3** are obtained by clamping the bottom and are shown in **Supplementary Figure 5**. It is observed that the labyrinthine inclusion gives higher stopbands in contrast to other two, i.e., 14.7 Hz for the labyrinthine steel inclusion in comparison with 12.7 and 11 Hz for split-ring and swiss-roll like steel inclusions.

We, next, investigate the effect of different soil properties, i.e., with soft soil having properties $E = 96.5$ MPa, $\mu = 0.33$, and $\rho = 1{,}650$ kg/m^3 and very soft soil type 1 with properties $E = 10$ MPa, $\mu = 0.25$, and $\rho = 1{,}400$ kg/m^3.

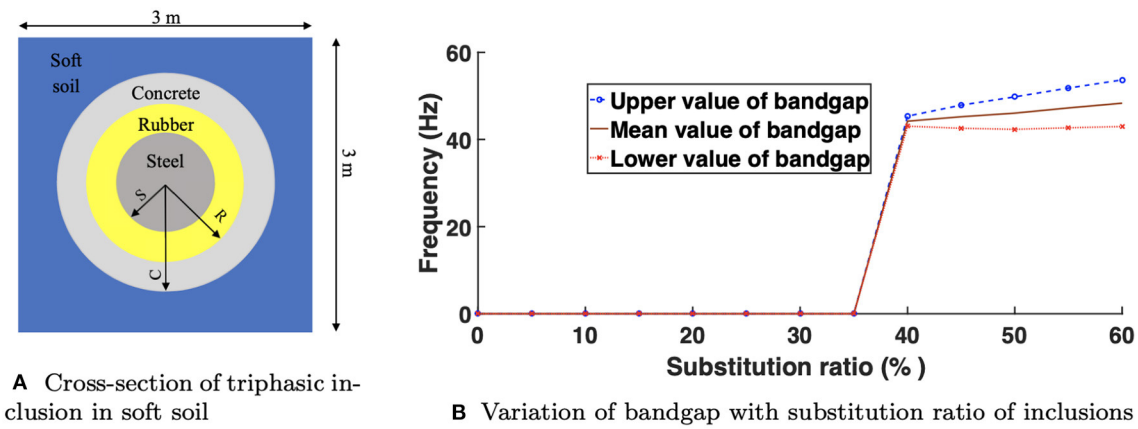

FIGURE 5 | Unclamped configuration (all three type of inclusion, i.e., concrete, rubber, and steel), and the variation of bandgap width vs. substitution ratio of triphasic inclusion in soft soil. The ratio of radius of each inclusion material for different substitution ratio is kept same, i.e., $\frac{S}{R} = \frac{R}{C} = 0.83$, where S, R, and C denote radius of steel, rubber, and concrete, respectively. The dimension of unit cell is $3 \times 3 \times 10$ m, and properties of soft soil is taken as $E = 96.5$ MPa, $\mu = 0.33$, and $\rho = 1{,}650$ kg/m^3. **(A)** Cross-section of triphasic inclusion in soft soil. **(B)** Variation of bandgap with substitution ratio of inclusions.

The labyrinthine and two gap split ring-like steel inclusions show an improvement on the width of the bandgaps obtained *via* dispersion curves in **Supplementary Figure 2**. The labyrinthine steel inclusion shows a bandgap of 6 Hz in the range of 38–44 Hz in soft soil (**Supplementary Figure 6a**) in contrast to medium soil (**Supplementary Figure 2b**) which shows no bandgap. The split ring with two gaps shows an enhanced bandgap (∼17 Hz) in soft soil with soil properties $E = 96.5$ MPa, $\mu = 0.33$, and $\rho = 1{,}650$ kg/m^3 (**Supplementary Figure 6b**). The bandgap is also obtained in a lower region than that obtained in the medium soil (**Supplementary Figure 2f**). On further exploring the soil properties, the two-gap split ring shows an excellent improvement over the bandgap in a very soft soil type 2 with soil properties $E = 5$ MPa, $\mu = 0.35$, and $\rho = 1{,}633$ kg/m^3. A bandgap of 5 Hz is obtained at a much lower region (∼8–13 Hz) in very soft soil type 2 for the two-gap split ring (**Supplementary Figure 6c**). Finally, we investigate a typical configuration, such as a triphasic inclusion as shown in **Figure 5** (Duplan et al., 2014). A circular cylinder of steel surrounded by a thick rubber shell that is surrounded by a concrete outer shell within a bulk of soft soil with parameters $E = 96.5$ MPa, $\mu = 0.33$, and $\rho = 1{,}650$ kg/m^3 as shown in **Figure 5A**. The ratio of radius of each inclusion material is taken, such as $S/R = R/C = 0.83$, where S, R, and C denote radius of steel, rubber, and concrete, respectively. The dimension of the unit cell is $3 \times 3 \times 10$ m. With increasing substitution ratio of material constituents, the varying bandgap width is plotted as shown in **Figure 5B**. We note that the lower (resp. upper) value of bandgap decreases (resp. increases) when substitution ratio increases from 40 to 60%, and thus the gap widens with increasing substitution ratio. It can be seen that the bandgap for triphasic inclusion appears at lower substitution rates than for monophasic substitution cases.

3.2. Effect of Varying Orientation in Square Inclusions

Having verified in subsection 3.1 that using a square geometry as the inclusion leads to better performance, here, we explore the effect of varying its orientation within the microstructure of

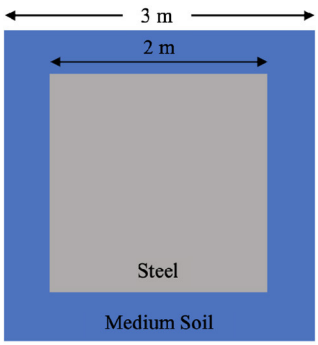

A Cross-section of 0° orientation of square inclusion with 0.445 substitution ratio

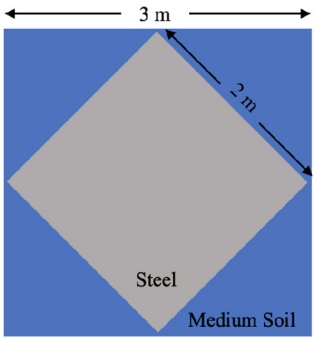

B Cross-section of 45° orientation of square inclusion with 0.445 substitution ratio

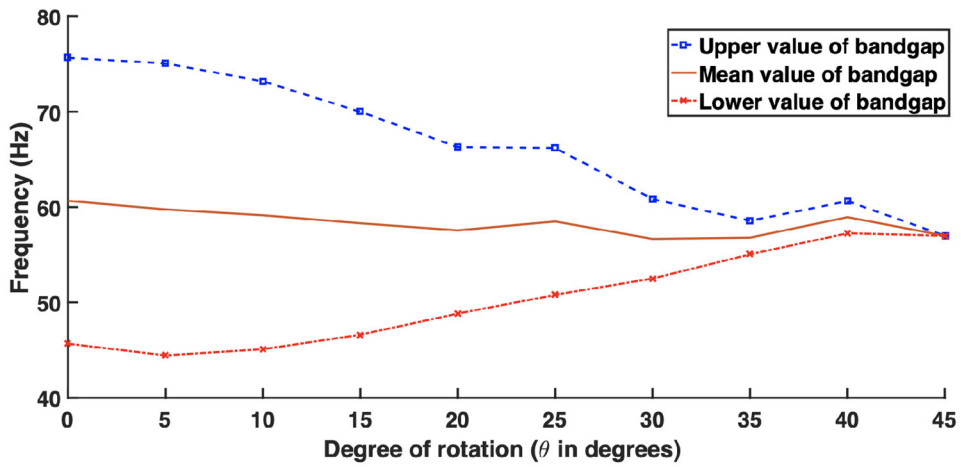

C Bandgap for unclamped configuration versus orientation angle (degree) plot for square inclusion (steel) in medium soil at same substitution ratio, i.e., 0.445

FIGURE 6 | Effect of change in orientation angle (in degrees) of unclamped regular-shaped square steel inclusion ($2 \times 2 \times 10$ m) with 0.445 substitution ratio in medium soil ($3 \times 3 \times 10$ m; $E = 153$ MPa, $\mu = 0.33$, and $\rho = 1{,}800$ kg/m^3) on bandgap; **(A,B)** show the cross-section of 0 and 45° angle orientation of unclamped square inclusion; and **(C)** shows the declining trend in bandgap with increase in angle from 0 to 45° in anticlockwise direction.

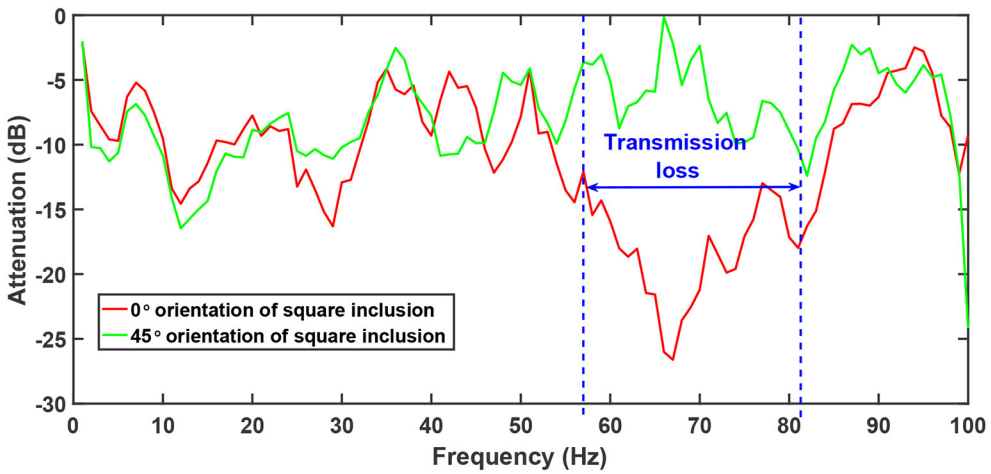

FIGURE 7 | Transmission spectra of 0 and 45° orientation of square steel inclusion in the medium soil matrix (bottom remains unclamped) are computed using a finite array of metamaterial design (corresponding to **Figure 6**). A dip is observed at ∼68 Hz, representing large wave attenuation.

periodic media by rotating it from 0 to 45°. With this exercise, we further explore the microstructure geometries toward achieving higher bandgaps. Steel inclusions are considered as the column with regular-shaped square geometry (2 × 2 × 10 m) within an unstructured medium soil (3 × 3 × 10 m), with properties the same as in section 3.1. The orientation of the square inclusion is made to vary from 0 to 45°, in increments of 5°. **Figure 6C** shows the plot for bandgaps obtained from varying the orientation of inclusion plotted against the angle. Interestingly, the plot shows a declining trend for the bandgap with increase in angle, starting from 28 Hz at 0° to 0 Hz at 45°. Thus, in summary a square inclusion oriented at 0° gives a wider bandgap in comparison to other orientations when examined with same substitution ratio. To further investigate the efficacy of the design, transmission losses (see **Figure 7**) are computed over a finite array of SM design consisting of five square steel columns (oriented at 0 and 45°, respectively). For the computation the Rayleigh wave is incident normally as a line source. With 0° orientation a dip is observed in the range of 58–82 Hz, which shows possible large wave attenuation/transmission loss, whereas no such observations is made for the 45° case. We did not foresee this result as this effect of the rotation on the stopband width is opposite to that observed for linear surface water propagating within a periodic structure consisting of rigid square inclusions (Farhat et al., 2008). Thus, one needs to be cautious when using analogies between surface water waves and Rayleigh waves.

3.3. Feasibility of Inclusion Material

So far we have discussed the geometry of the inclusions within the unit cell, so as to generate a wide bandgap and its positioning in the frequency spectrum. However, we have exclusively utilized steel as the constituent material of the inclusion. But it is not feasible, either economically and technically, to generate such a large volume of steel having dimensions 2 × 2 × 10 m making up a volume of 40 m^3 and then to give them complex cross-section geometry *via* standard industrial fabrication processes. Conversely, concrete has an advantage over steel, in terms of fire and corrosion resistance, low density, resistant to impact of high groundwater level, and other on-field applications like being easily moldable into desired shapes, and these considerations make it a better choice within the civil engineering domain. Noting this fact, we compared the dispersion properties of concrete inclusions (M50 grade) with that of steel inclusions (**Figures 3D**, **8B**); both having the same substitution ratio (0.445) and embedded in medium soil whose geometry and elastic properties are same as in section 3.1. The elastic properties of M50 grade concrete is taken as E = 35.35 GPa, Poisson's ratio, μ = 0.15, and density, ρ = 2,400 kg/m^3. Unfortunately, concrete inclusions in a medium soil matrix show no bandgap frequencies (**Figure 8B**). However, as discussed earlier, concrete is an ideal choice for most of the civil installations, and so we performed a parametric study with different grades of concrete combined with soft, medium, and dense soil. In the process of which, we arrive at a design of SM having M50 grade concrete inclusion in very soft soil type 1 (soil properties is taken as E = 10 MPa, Poisson's ratio, μ = 0.25, and density, ρ = 1,400 kg/m^3), showing a bandgap of ∼3.91 Hz in the range of 18.45–22.36 Hz (**Figure 8D**). Transmission losses are computed using a finite strip of five concrete square columns in very soft soil type 1 which shows large Rayleigh wave attenuation in the range of 15–25 Hz, in comparison to the medium soil (**Figure 9**). Zero frequency stopband computation (see **Figure 10**) distinctly shows two bandgaps; ultra-low stopband frequency (0–7.62 Hz) and a higher range of bandgap, ∼3.28 Hz (range 18.72–22 Hz). Transmission loss for 0° oriented regular-shaped square concrete columns in very soft soil type 1 (E = 10 MPa, μ = 0.25, and ρ = 1,400 kg/m^3) and medium (E = 153 MPa, μ = 0.3, and ρ = 1,800 kg/m^3) soil matrix is also computed over a finite array of the design region (see **Figure 11**). Clearly, concrete columns in soft soil type 1 attenuates the Rayleigh wave

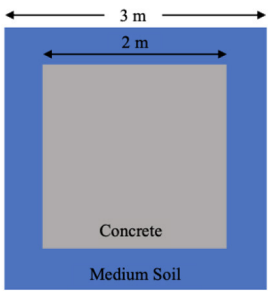

A Concrete inclusion in medium soil matrix with 0.445 susbtitution ratio

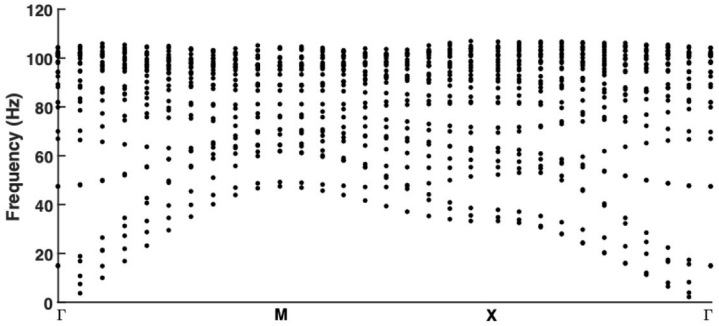

B Dispersion curves for square inclusion in medium soil

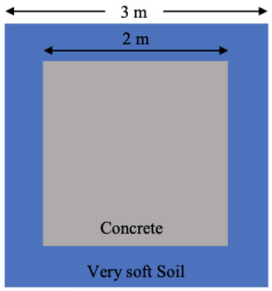

C Concrete inclusion in very soft soil matrix with 0.445 susbtitution ratio

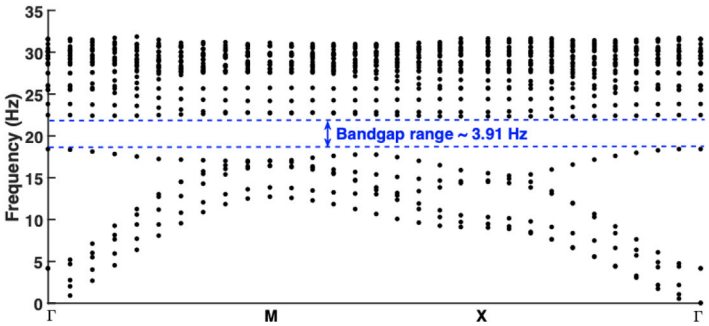

D Dispersion curves for square inclusion in loose soil

FIGURE 8 | Unclamped configuration of concrete inclusion (with 0.445 substitution ratio) in **(A)** medium soil ($E = 153$ MPa, $\mu = 0.33$, and $\rho = 1{,}800$ kg/m^3); **(C)** very soft soil ($E = 10$ MPa, $\mu = 0.25$, and $\rho = 1{,}400$ kg/m^3). Corresponding dispersion curves obtained are shown in **(B,D)**, around the edges of the irreducible Brillouin zone Γ*XM*. No bandgap is observed with the medium soil matrix; whereas in very soft soil a bandgap, ~3.91 Hz, is observed.

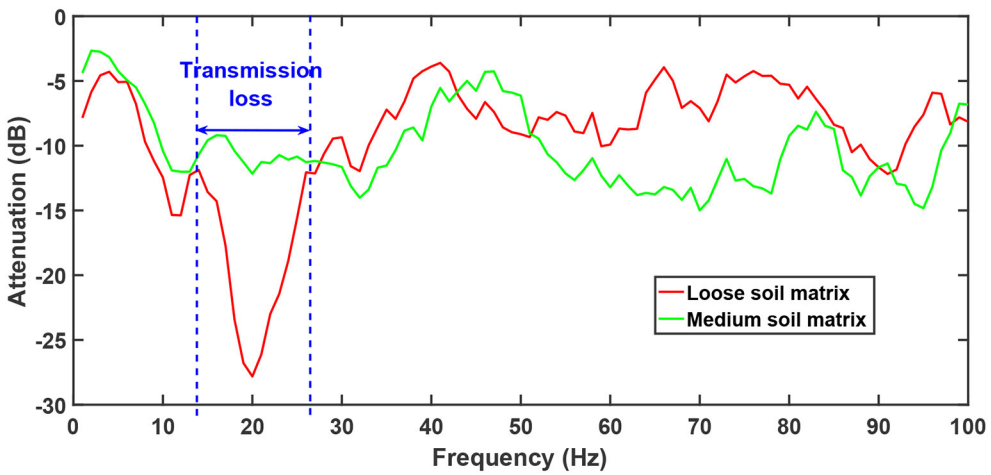

FIGURE 9 | Transmission losses for unclamped concrete inclusions (2 × 2 × 10 m) in very soft soil type 1 (E = 10 MPa, $\mu = 0.25$, and $\rho = 1{,}400$ kg/m^3) and medium soil (E = 153 MPa, $\mu = 0.33$, and $\rho = 1{,}800$ kg/m^3) matrix (3 × 3 × 10 m) corresponding to **Figure 8**. The substitution ratio is kept same, i.e., 0.445. Notably, square concrete inclusions in very soft soil type 1 show attenuation in the bandgap range, i.e., 18.45–22.36 Hz.

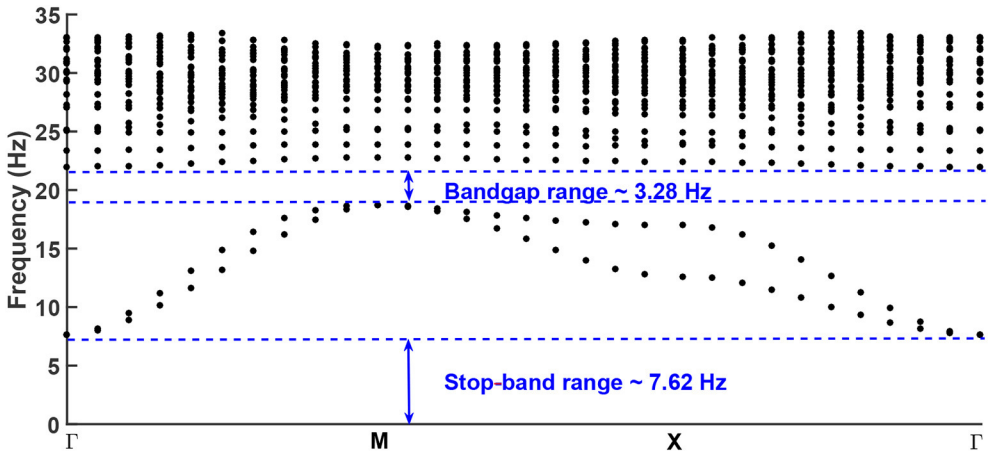

FIGURE 10 | Dispersion curve for clamped configuration of M50 grade square concrete columns (2 × 2 × 10 m) in soft soil matrix (3 × 3 × 10 m; $E = 10$ MPa, $\mu = 0.25$, and $\rho = 1{,}400$ kg/m^3) (substitution ratio 0.445). Two bandgaps were observed; a stopband of 7.62 Hz and a bandgap in the range of 18.72–22 Hz.

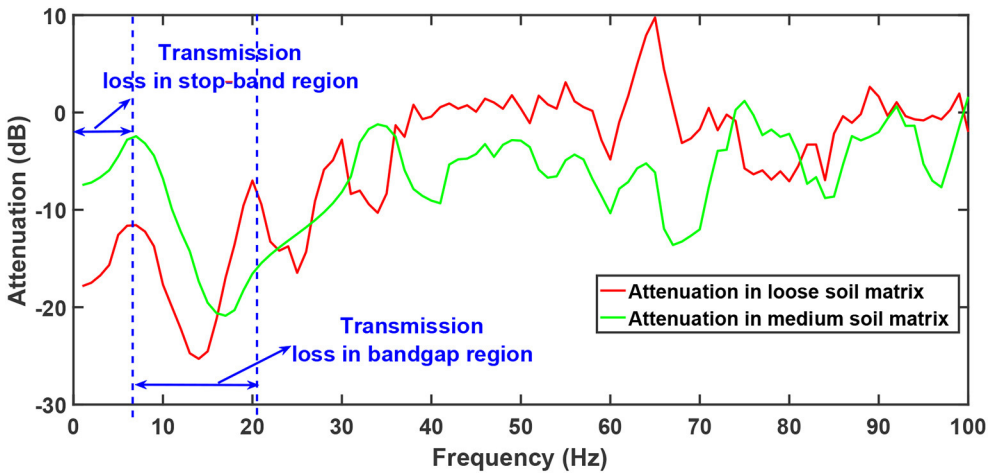

FIGURE 11 | Attenuation for clamped configuration of square concrete columns having dimension 2 × 2 × 10 m in soft soil type 1 (E = 10 MPa, $\mu = 0.25$, and $\rho = 1{,}400$ kg/m^3) and medium soil (E = 153 MPa, $\mu = 0.33$, and $\rho = 1{,}800$ kg/m^3) matrix having dimension 3 × 3 × 10 m (substitution ratio 0.445). Clearly, loss in soft soil type 1 matrix is more in comparison to medium soil.

vibrations to a larger extent in comparison to medium soil matrix in stopband.

As mentioned earlier, since loose soil is not suitable for construction purposes, we recommend the following architecture. As shown in **Figure 12**, for a finite region to be protected (denoted with A in **Figure 12**), the SM microstructure should be designed using square inclusions of concrete columns oriented at 0° in a narrow strip of very soft soil matrix denoted with orange color in **Figure 12**, leaving the residual region in its natural/structured state, making civil constructions possible on the residual region. Another aspect is that since the civil installations within the protected region may vary largely, with varied natural frequency range and importance, concrete columns of such a high dimension may not be necessary always. For the same, a parametric study on obtaining stopbands with different concrete sizes is performed, and the results are shown in **Figure 13**. The effect of variation of stopband follows a linear trend with increasing substitution ratio of regular-shaped square concrete columns. Such graphs can be used for calibration purpose for optimal SM design.

4. CONCLUSIONS

In this paper, we have first noticed the importance of structure geometry to further enhance the filtering effects of clamped seismic metamaterials consisting of cylindrical inertial resonators clamped at their bottom. The clamping makes possible a

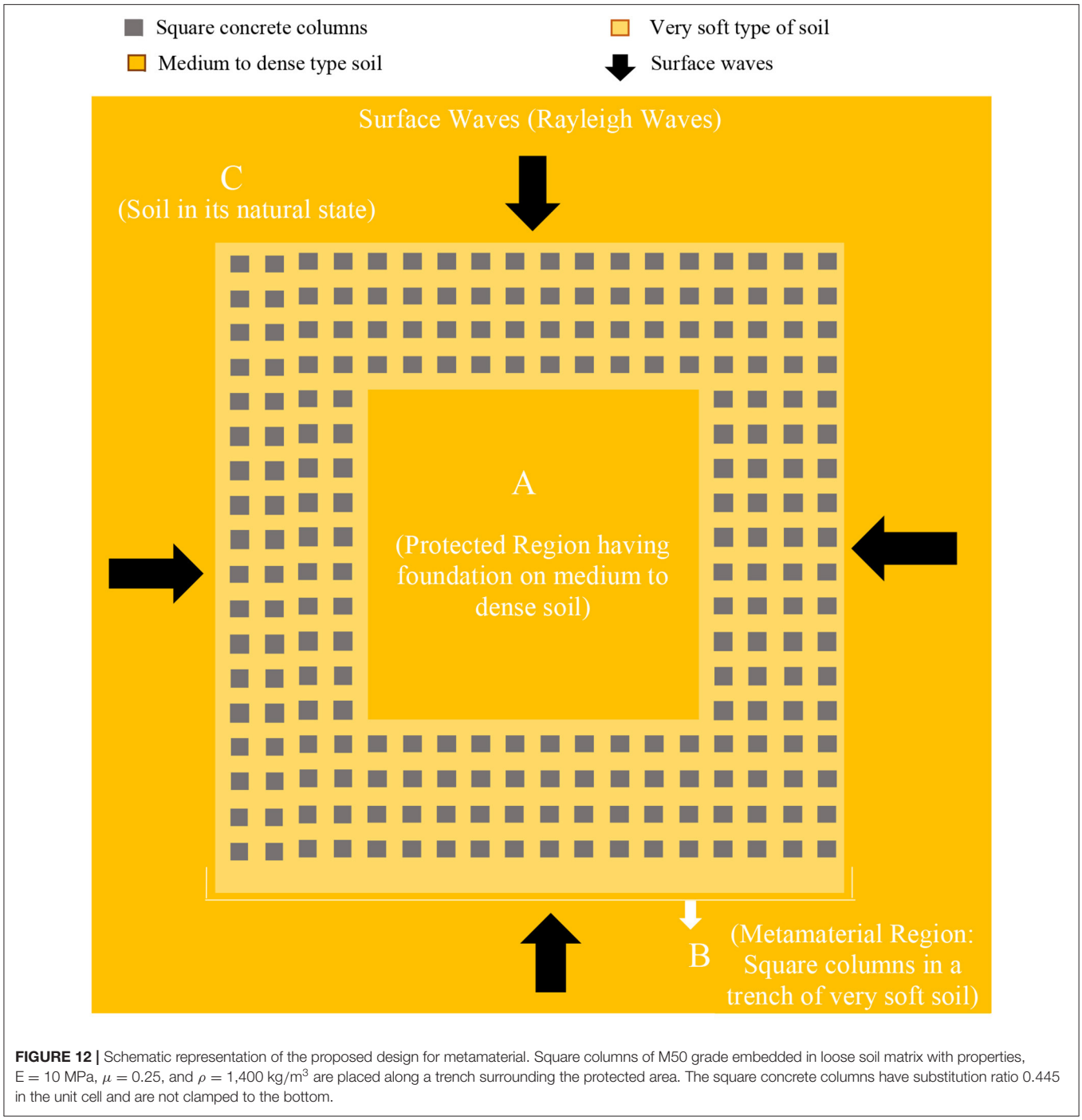

FIGURE 12 | Schematic representation of the proposed design for metamaterial. Square columns of M50 grade embedded in loose soil matrix with properties, E = 10 MPa, $\mu = 0.25$, and $\rho = 1{,}400$ kg/m^3 are placed along a trench surrounding the protected area. The square concrete columns have substitution ratio 0.445 in the unit cell and are not clamped to the bottom.

zero-frequency stopband of interest for earthquake protection, whereas the microstructure allows for additional stopbands at higher frequencies that might find applications in suppression of ground vibrations induced by traffic. We stress that such types of cylindrical inclusions mixing stress-free and clamped boundary conditions have no counterpart in electromagnetism since these conditions model infinite conducting inclusions in irreconcilable light polarizations (transverse electric and magnetic fields, for stress-free and clamped conditions, respectively). We have explored the effect of different microstructure geometries of SMs toward obtaining a wider bandgap with equal amount of inclusions and its positioning in frequency spectrum, i.e., a lower bandgap region (approximately below 20 Hz) is essential for most of the engineering applications. We have arrived at a configuration of columns having a square cross-section with sides aligned with a square lattice that gives a wider

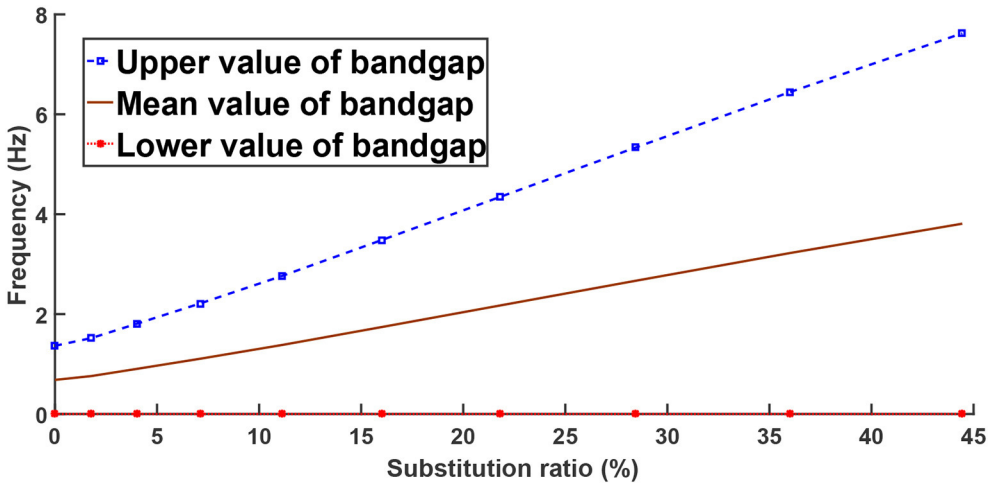

FIGURE 13 | Bandgap vs. substitution ratio plot for clamped configuration of square concrete inclusion in a unit cell of dimension 3 × 3 m. The soil properties are taken as E = 10 MPa, $\mu = 0.25$, and $\rho = 1{,}400$ kg/m^3.

bandgap in comparison to circular cross-section inclusions for the same substitution ratio of constituent material. This has been demonstrated by computing transmission losses in addition to the dispersion curves for different microstructure geometries of the SM. We have also performed analysis of the constituent material, observing that, not only steel, but concrete the conventional construction material, can also be used to design inclusions for large wave attenuation. This is important for the industrial scale-up of the technology because, concrete is cost effective, easy to cast directly at the construction site, and easy to provide arbitrary geometry of the microstructure. We have observed that concrete shows a bandgap for very soft soil. Since, very soft soil is not suitable for constructions, we prescribe an architecture of SM, with concrete inclusions in a narrow strip of very soft soil matrix surrounding the protected region. Even though we have arrived at an efficient design of SM, our study opens the door to further generalization. For example, we assume linear elastic materials, and it would be interesting to see what happens in case of material and geometric non-linearity; soil often shows a significant amount of plastic deformation. In a future study, we would like to pay more attention to damping of ground vibrations, introducing so-called K-Dampers, such as those used to reduce vibration of bridges (Sapountzakis et al., 2018) and to mitigate of site-city interactions (Ungureanu et al., 2019) using the SMs which we introduced here.

DATA AVAILABILITY STATEMENT

The original contributions presented in the study are included in the article/**Supplementary Material**, further inquiries can be directed to the corresponding author/s.

AUTHOR CONTRIBUTIONS

All authors listed have made a substantial, direct and intellectual contribution to the work, and approved it for publication.

ACKNOWLEDGMENTS

SS acknowledges Ravi Sharma and Anshul Srivastava (IIT Indore, B.Tech. batch 2020) for helping him in some initial simulations at the preliminary stage of this work. BU acknowledges funding from European Union (MARIE SKODOWSKA-CURIE ACTIONS project Acronym/Full Title: METAQUAKENG—Metamaterials in Earthquake Engineering—MSCA IF—H2020).

SUPPLEMENTARY MATERIAL

The Supplementary Material for this article can be found online at: https://www.frontiersin.org/articles/10.3389/fmats.2021.603820/full#supplementary-material

REFERENCES

Achaoui, Y., Antonakakis, T., Brule, S., Craster, R., Enoch, S., and Guenneau, S. (2017). Clamped seismic metamaterials: ultra-low frequency stop bands. *New J. Phys.* 19:063022. doi: 10.1088/1367-2630/aa6e21

Achenbach, J. D. (1973). *Wave Propagation in Elastic Solids*. Amsterdam: Elsevier.

Anajafi, H., and Medina, R. A. (2018). Comparison of the seismic performance of a partial mass isolation technique with conventional tmd and base-isolation systems under broad-band and narrow-band excitations. *Eng. Struct.* 158, 110–123. doi: 10.1016/j.engstruct.2017.12.018

Aravantinos-Zafiris, N., and Sigalas, M. (2015). Large scale phononic metamaterials for seismic isolation. *J. Appl. Phys.* 118:064901. doi: 10.1063/1.4928405

Bajcar, T., Cimerman, F., Širok, B., and Ameršek, M. (2012). Impact assessment of traffic-induced vibration on natural gas transmission pipeline. *J. Loss Prev. Process Ind.* 25, 1055–1068. doi: 10.1016/j.jlp.2012.07.021

Bigoni, D., Guenneau, S., Movchan, A., and Brun, M. (2013). Elastic metamaterials with inertial locally resonant structures: application to lensing and localization. *Phys. Rev. B* 87:174303. doi: 10.1103/PhysRevB.87.174303

Brillouin, L. (2003). *Wave Propagation in Periodic Structures: Electric Filters and Crystal Lattices*. New York, NY: Courier Corporation.

Brownjohn, J. M., De Stefano, A., Xu, Y.-L., Wenzel, H., and Aktan, A. E. (2011). Vibration-based monitoring of civil infrastructure: challenges and successes. *J. Civil Struct. Health Monit*. 1, 79–95. doi: 10.1007/s13349-011-0009-5

Brûlé, S., Enoch, S., and Guenneau, S. (2018a). Experimental evidence of auxetic features in seismic metamaterials: ellipticity of seismic Rayleigh waves for subsurface architectured ground with holes. *arXiv* 1809.05841.

Brûlé, S., Enoch, S., and Guenneau, S. (2019). Role of nanophotonics in the birth of seismic megastructures. *Nanophotonics* 8, 1591–1605. doi: 10.1515/nanoph-2019-0106

Brûlé, S., Enoch, S., and Guenneau, S. (2020). Emergence of seismic metamaterials: current state and future perspectives. *Phys. Lett. A* 384:126034. doi: 10.1016/j.physleta.2019.126034

Brûlé, S., Enoch, S., Guenneau, S., and Craster, R. (2018b). *Seismic Metamaterials: Controlling Surface Rayleigh Waves Using Analogies With Electromagnetic Metamaterials. Handbook of Metamaterials*. Singapore: World Scientific.

Brûlé, S., and Guenneau, S. (2019). The role of seismic metamaterials on soil dynamics. *arXiv* 1912.12916.

Brûlé, S., Javelaud, E., Enoch, S., and Guenneau, S. (2014). Experiments on seismic metamaterials: molding surface waves. *Phys. Rev. Lett*. 112:133901. doi: 10.1103/PhysRevLett.112.133901

Brûlé, S., Javelaud, E. H., Enoch, S., and Guenneau, S. (2017a). Flat lens effect on seismic waves propagation in the subsoil. *Sci. Rep*. 7:18066. doi: 10.1038/s41598-017-17661-y

Brûlé, S., Ungureanu, B., Achaoui, Y., Diatta, A., Aznavourian, R., Antonakakis, T., et al. (2017b). Metamaterial-like transformed urbanism. *Innov. Infrastruct. Solut*. 2:20. doi: 10.1007/s41062-017-0063-x

Casablanca, O., Ventura, G., Garescì, F., Azzerboni, B., Chiaia, B., Chiappini, M., et al. (2018). Seismic isolation of buildings using composite foundations based on metamaterials. *J. Appl. Phys*. 123:174903. doi: 10.1063/1.5018005

Chestler, S., and Creager, K. (2017). Evidence for a scale-limited low-frequency earthquake source process. *J. Geophys. Res. Solid Earth* 122, 3099–3114. doi: 10.1002/2016JB013717

Colombi, A., Colquitt, D., Roux, P., Guenneau, S., and Craster, R. V. (2016). A seismic metamaterial: the resonant metawedge. *Sci. Rep*. 6:27717. doi: 10.1038/srep27717

Colombi, A., Craster, R. V., Colquitt, D., Achaoui, Y., Guenneau, S., Roux, P., et al. (2017). Elastic wave control beyond band-gaps: shaping the flow of waves in plates and half-spaces with subwavelength resonant rods. *Front. Mech. Eng*. 3:10. doi: 10.3389/fmech.2017.00010

Craster, R. V., and Guenneau, S. (2012). *Acoustic Metamaterials: Negative Refraction, Imaging, Lensing and Cloaking*, Vol. 166. London: Springer Science & Business Media.

Del Vescovo, D., and Giorgio, I. (2014). Dynamic problems for metamaterials: review of existing models and ideas for further research. *Int. J. Eng. Sci*. 80, 153–172. doi: 10.1016/j.ijengsci.2014.02.022

Diatta, A., Achaoui, Y., Brûlé, S., Enoch, S., and Guenneau, S. (2016). Control of Rayleigh-like waves in thick plate Willis metamaterials. *AIP Adv*. 6:121707. doi: 10.1063/1.4972280

Duplan, F., Abou-Chakra, A., Turatsinze, A., Escadeillas, G., Brûlé, S., and Masse, F. (2014). Prediction of modulus of elasticity based on micromechanics theory and application to low-strength mortars. *Construct. Build. Mater*. 50, 437–447. doi: 10.1016/j.conbuildmat.2013.09.051

Dym, C. L. (2012). Approximating frequencies of tall buildings. *J. Struct. Eng*. 139, 288–293. doi: 10.1061/(ASCE)ST.1943-541X.0000656

Dym, C. L., and Williams, H. E. (2007). Estimating fundamental frequencies of tall buildings. *J. Struct. Eng*. 133, 1479–1483. doi: 10.1061/(ASCE)0733-9445(2007)133:10(1479)

Economou, E., and Sigalas, M. (1993). Classical wave propagation in periodic structures: cermet versus network topology. *Phys. Rev. B* 48:13434. doi: 10.1103/PhysRevB.48.13434

Fabrizio, C., de Leo, A. M., and Di Egidio, A. (2019). Tuned mass damper and base isolation: a unitary approach for the seismic protection of conventional frame structures. *J. Eng. Mech*. 145:04019011. doi: 10.1061/(ASCE)EM.1943-7889.0001581

Farhat, M., Guenneau, S., Enoch, S., Tayeb, G., Alexander, M., and Natasha, M. (2008). Analytical and numerical analysis of lensing effect for linear surface water waves through a square array of nearly touching rigid square cylinders. *Phys. Rev. E* 77:046308. doi: 10.1103/PhysRevE.77.046308

Frenzel, T., Kopfler, J., Jung, E., Kadic, M., and Wegener, M. (2019). Ultrasound experiments on acoustical activity in chiral mechanical metamaterials. *Nat. Commun*. 10:3384. doi: 10.1038/s41467-019-11366-8

Gadallah, M. R., and Fisher, R. L. (2005). *Applied Seismology: A Comprehensive Guide to Seismic Theory and Application*. Okhlahoma: PennWell Books.

Gazalet, J., Dupont, S., Kastelik, J., Rolland, Q., and Djafari-Rouhani, B. (2013). A tutorial survey on waves propagating in periodic media: electronic, photonic and phononic crystals. Perception of the Bloch theorem in both real and fourier domains. *Wave Motion* 50, 619–654. doi: 10.1016/j.wavemoti.2012.12.010

Gómez-León, A., and Platero, G. (2013). Floquet-Bloch theory and topology in periodically driven lattices. *Phys. Rev. Lett*. 110:200403. doi: 10.1103/PhysRevLett.110.200403

Guenneau, S., and Movchan, A. (2004). Analysis of elastic band structures for oblique incidence. *Archiv. Ration. Mech. Anal*. 171, 129–150. doi: 10.1007/s00205-003-0288-z

Guenneau, S., Movchan, A., Pétursson, G., and Ramakrishna, S. A. (2007). Acoustic metamaterials for sound focusing and confinement. *New J. Phys*. 9:399. doi: 10.1088/1367-2630/9/11/399

Harvey, P. S. Jr., and Kelly, K. C. (2016). A review of rolling-type seismic isolation: historical development and future directions. *Eng. Struct*. 125, 521–531. doi: 10.1016/j.engstruct.2016.07.031

Jarlebring, E., Mele, G., and Runborg, O. (2017). The waveguide eigenvalue problem and the tensor infinite Arnoldi method. *SIAM J. Sci. Comput*. 39, A1062–A1088. doi: 10.1137/15M1044667

Kadic, M., Buckmann, T., Schittny, R., and Wegener, M. (2013). Metamaterials beyond electromagnetism. *Rep. Prog. Phys*. 76:126501. doi: 10.1088/0034-4885/76/12/126501

Kadic, M., Diatta, A., Frenzel, T., Guenneau, S., and Wegener, M. (2019). Static chiral willis continuum mechanics for three-dimensional chiral mechanical metamaterials. *Phys. Rev. B* 99:214101. doi: 10.1103/PhysRevB.99.214101

Kramer, S. L. (2007). *Geotechnical Earthquake Engineering*. New Jersey: Pearson Education, Inc.

Lee, H. M., and Wu, J. C. (2010). Transmittance spectra in one-dimensional superconductor-dielectric photonic crystal. *J. Appl. Phys*. 107:09E149. doi: 10.1063/1.3362935

Liu, Y., Huang, J., Li, Y., and Shi, Z. (2019). Trees as large-scale natural metamaterials for low-frequency vibration reduction. *Construct. Build. Mater*. 199, 737–745. doi: 10.1016/j.conbuildmat.2018.12.062

Mandelik, D., Eisenberg, H., Silberberg, Y., Morandotti, R., and Aitchison, J. (2003). Band-gap structure of waveguide arrays and excitation of Floquet-Bloch solitons. *Phys. Rev. Lett*. 90:053902. doi: 10.1103/PhysRevLett.90.053902

Meseguer, F., Holgado, M., Caballero, D., Benaches, N., Lopez, C., Sanchez-Dehesa, J., et al. (1999a). Two-dimensional elastic bandgap crystal to attenuate surface waves. *J. Lightw. Technol*. 17, 2196–2201. doi: 10.1109/50.803011

Meseguer, F., Holgado, M., Caballero, D., Benaches, N., Sánchez-Dehesa, J., López, C., et al. (1999b). Rayleigh-wave attenuation by a semi-infinite two-dimensional elastic-band-gap crystal. *Phys. Rev. B* 59:12169. doi: 10.1103/PhysRevB.59.12169

Miniaci, M., Krushynska, A., Bosia, F., and Pugno, N. M. (2016). Large scale mechanical metamaterials as seismic shields. *New J. Phys*. 18:083041. doi: 10.1088/1367-2630/18/8/083041

Moitra, P., Slovick, B. A., Li, W., Kravchencko, I. I., Briggs, D. P., Krishnamurthy, S., et al. (2015). Large-scale all-dielectric metamaterial perfect reflectors. *ACS Photon*. 2, 692–698. doi: 10.1021/acsphotonics.5b00148

Mosby, M., and Matouš, K. (2016). Computational homogenization at extreme scales. *Extreme Mech. Lett*. 6, 68–74. doi: 10.1016/j.eml.2015.12.009

Moser, P., and Moaveni, B. (2011). Environmental effects on the identified natural frequencies of the dowling hall footbridge. *Mech. Syst. Signal Process*. 25, 2336–2357. doi: 10.1016/j.ymssp.2011.03.005

Muhammad and Lim, C. (2019). Elastic waves propagation in thin plate metamaterials and evidence of low frequency pseudo and local resonance bandgaps. *Phys. Lett. A* 383, 2789–2796. doi: 10.1016/j.physleta.2019.05.039

Nakano, M., Hori, T., Araki, E., Kodaira, S., and Ide, S. (2018). Shallow very-low-frequency earthquakes accompany slow slip events in the Nankai subduction zone. *Nat. Commun.* 9:984. doi: 10.1038/s41467-018-03431-5

Palermo, A., Krödel, S., Marzani, A., and Daraio, C. (2016). Engineered metabarrier as shield from seismic surface waves. *Sci. Rep*. 6:39356. doi: 10.1038/srep39356

Pendry, J., Holden, A., Robbins, D., and Stewart, W. (1999). Magnetism from conductors and enhanced nonlinear phenomena. *IEEE Trans. Microw. Theory Tech*. 47, 2075–2084. doi: 10.1109/22.798002

Poddubny, A., Iorsh, I., Belov, P., and Kivshar, Y. (2013). Hyperbolic metamaterials. *Nat. Photon*. 7:948. doi: 10.1038/nphoton.2013.243

Reddy, J. N. (1993). *An Introduction to the Finite Element Method*. New York, NY: McGraw-Hill Education.

Sapountzakis, E., Syrimi, P., and Antoniadis, I. (2018). Engineered metabarrier as shield from seismic surface waves. *Int. J. Geoeng. Case Hist*. 4, 289–305. doi: 10.4417/IJGCH-04-04-05

Sun, F., and Xiao, L. (2019). Bandgap characteristics and seismic applications of inerter-in-lattice metamaterials. *J. Eng. Mech*. 145:04019067. doi: 10.1061/(ASCE)EM.1943-7889.0001642

Ungureanu, B., Achaoui, Y., Enoch, S., Brûlé, S., and Guenneau, S. (2015). Auxetic-like metamaterials as novel earthquake protections. *arXiv* 1510.08785. doi: 10.1051/epjam/2016001

Ungureanu, B., Guenneau, S., Achaoui, Y., Diatta, A., Farhat, M., Hutridurga, H., et al. (2019). The influence of building interactions on seismic and elastic body waves. *EPJ Appl. Metamater*. 6:18. doi: 10.1051/epjam/2019015

Van Der Aa, N., Ter Morsche, H., and Mattheij, R. (2007). Computation of eigenvalue and eigenvector derivatives for a general complex-valued eigensystem. *Electron. J. Linear Algebra* 16:26. doi: 10.13001/1081-3810.1203

Wagner, P. R., Dertimanis, V. K., Chatzi, E. N., and Beck, J. L. (2017). Robust-to-uncertainties optimal design of seismic metamaterials. *J. Eng. Mech*. 144:04017181. doi: 10.1061/(ASCE)EM.1943-7889.0001404

Wang, P., Casadei, F., Shan, S., Weaver, J., and Bertoldi, K. (2014). Harnessing buckling to design tunable locally resonant acoustic metamaterials. *Phys. Rev. Lett*. 113:014301. doi: 10.1103/PhysRevLett.113.014301

Wang, P., Lu, L., and Bertoldi, K. (2015). Topological phononic crystals with one-way elastic edge waves. *Phys. Rev. Lett*. 115, 104302. doi: 10.1103/PhysRevLett.115.104302

Watts, C. M., Liu, X., and Padilla, W. J. (2012). Metamaterial electromagnetic wave absorbers. *Adv. Mater*. 24, OP98–OP120. doi: 10.1002/adma.201200674

Xiang, H., Shi, Z., Wang, S., and Mo, Y. (2012). Periodic materials-based vibration attenuation in layered foundations: experimental validation. *Smart Mater. Struct*. 21:112003. doi: 10.1088/0964-1726/21/11/112003

Xiang, P., and Nishitani, A. (2014). Seismic vibration control of building structures with multiple tuned mass damper floors integrated. *Earthq. Eng. Struct. Dyn*. 43, 909–925. doi: 10.1002/eqe.2379

Yang, Y., Wang, H., Yu, F., Xu, Z., and Chen, H. (2016). A metasurface carpet cloak for electromagnetic, acoustic and water waves. *Sci. Rep*. 6:20219. doi: 10.1038/srep20219

Yao, J., Zhao, R., Zhang, N., and Yang, D. (2019). Vibration isolation effect study of in-filled trench barriers to train-induced environmental vibrations. *Soil Dyn. Earthq. Eng*. 125:105741. doi: 10.1016/j.soildyn.2019.105741

Zeng, Y., Xu, Y., Yang, H., Muzamil, M., Xu, R., Deng, K., et al. (2020). A matryoshka-like seismic metamaterial with wide band-gap characteristics. *Int. J. Solids Struct*. 185, 334–341. doi: 10.1016/j.ijsolstr.2019.08.032

Zhang, J., Liang, Z., Feng, D., Zhang, C., Xia, C., and Tu, Y. (2016). Response of the buried steel pipeline caused by perilous rock impact: parametric study. *J. Loss Prev. Process Ind*. 43, 385–396. doi: 10.1016/j.jlp.2016.06.019

Zhou, X., Yan, W., and Yang, R. (2002). Seismic base isolation, energy dissipation and vibration control of building structures. *J. Build. Struct*. 23, 2–13. Available online at: https://en.cnki.com.cn/Article_en/CJFDTotal-JZJB200202000.htm

Conflict of Interest: The authors declare that the research was conducted in the absence of any commercial or financial relationships that could be construed as a potential conflict of interest.